Chapter 8

Lithium Niobate Optical Waveguides and Microwaveguides

Nadège Courjal, Maria-Pilar Bernal, Alexis Caspar, Gwenn Ulliac, Florent Bassignot, Ludovic Gauthier-Manuel and Miguel Suarez

Additional information is available at the end of the chapter

http://dx.doi.org/10.5772/intechopen.76798

Abstract

Lithium niobate has attracted much attention since the 1970s due to its capacity to modify the light by means of an electric control. In this chapter, we review the evolution of electro-optical (EO) lithium niobate waveguides throughout the years, from Ti-indiffused waveguides to photonic crystals. The race toward ever smaller EO components with ever-lower optical losses and power consumption has stimulated numerous studies, the challenge consisting of strongly confining the light while preserving low losses. We show how waveguides have evolved toward ridges or thin film-based microguides to increase the EO efficiency and reduce the driving voltage. In particular, a focus is made on an easy-to-implement technique using a circular precision saw to produce thin ridge waveguides or suspended membranes with low losses.

Keywords: integrated optics, $LiNbO_3$, electro-optics, optical grade dicing, photonics

1. Introduction

The electric control of light has fascinated people since the advent of electricity. The advent of cleanroom technologies in the early 1940s and the advances in fabrication technologies in the 1950s and 1960s have progressively opened up pathways toward integrated optics, offering the possibility of guiding light in small devices while controlling its flux. In this context, lithium niobate, also named $LiNbO_3$, has always played a prominent role. Indeed its refractive index—which governs the speed of light—is sensitive to electrical signals, thanks to its

electro-optical (EO) properties [1]. Hence, $LiNbO_3$ is often used when light modulation is required, as for example in fiber optic-based telecommunication systems.

As compared with semiconductors modulating electrically the absorption of light through the Franz-Keldysh effect, $LiNbO_3$-based modulators can change light intensity without any perturbation on the phase, that is, without chirp. Therefore, despite the great success of semiconductors for short-range telecommunication systems, the zero-chirp modulation provided by $LiNbO_3$-based components is still privileged when high-bit rate optical signals have to propagate through thousands of kilometers [2].

In comparison with polymers [3] or other ferroelectrics such as SBN [4], KTN [5], $BaTiO_3$ [6], which show even higher EO sensitivity than $LiNbO_3$, the material benefits from technological maturity based on Czochralski's process, so that numerous suppliers can be found around the world. Moreover, its physical properties are compatible with cleanroom fabrication processes. For example, its high Curie temperature (~ 1200°C) preserves the EO properties even during annealing steps, which is not the case for materials like SBN or KTN. Additionally, $LiNbO_3$ offers a wide transparency band [340–4.6 μm] which opens the range to applications from visible to mid-infrared. The low absorption losses (< 0.15%/cm at 1.06 μm) and its weak optical dispersion in the transparency band [7] also contribute to its success. As a result, lithium niobate has become indispensable for demanding applications such as broadband modulation for long-haul high-bit-rate optical telecommunication systems [2, 8], electromagnetic sensors [9], precision gyroscopes [10], and astronomy [11]. For each application, the challenge is to provide integrated configurations that are easy to implement, of low loss, low in energy consumption, and, if possible, compact. The basic element, namely the optical waveguide, is essential to meet these specifications.

First, we will provide some reminders about the classic electro-optical configurations. Then we will see the evolutions of $LiNbO_3$ optical waveguides from their first appearance in the 1970s to recent evolutions. Finally, we will show how nanoscale structuring can open up new perspectives for the material.

2. Electro-optical configurations in lithium niobate

The technological evolutions concerning electrooptical $LiNbO_3$ waveguides are oriented toward ever-lower propagation losses and lower coupling losses with fibers, while also seeking ever higher EO efficiency. The common specifications are summarized in Refs. [10, 12]. In what follows, we will take particular interest in optical losses and EO efficiency. Beforehand, we provide a quick reminder of the exploitation of the EO effect in lithium niobate.

$LiNbO_3$ EO modulators exploit the classic Pockels effect, which corresponds to a linear change of the refractive index as a function of the applied voltage. This index modification is due to the relative displacement of charges in the presence of an electric field $\vec{E}\ (E_1, E_2, E_3)$, which induces a macroscopic polarization inside the material. The modified index n'_i can be deduced

http://dx.doi.org/10.5772/intechopen.76798

from the intrinsic refractive index n_i and the electrooptic tensor [r] by using Eq.(1) in the crystalline coordinate system:

$$\frac{1}{n_i'^2} = \frac{1}{n_i^2} + \sum_{j=1}^{3} r_{ij} E_j \tag{1}$$

The non-zero electrooptical coefficients r_{13}, r_{51}, r_{33}, and r_{22} of the [r] tensor are summarized in **Table 1** at 1550 nm wavelength for $LiNbO_3$ crystal substrates.

As r_{33} is the highest electro-optic coefficient of the material, the most efficient EO configuration is achieved when both the electric field and the optical polarization are parallel with the third crystalline axis, that is, the Z-axis. This can be accomplished either by X-cut Y-propagating or by Z-cut waveguides. In what follows, we will mainly focus on X-cut waveguides (see **Figure 1**), which show better thermal stability than Z-cut ones.

In an X-cut Y-propagating waveguide, the crystalline X-axis is vertical, the Z-axis is in the plan of the wafer, and a waveguide is implemented along the Y-axis. Coplanar electrodes are placed on both sides of the waveguide (see **Figure 1**), and the gap g between them is kept the same along the Y-axis. Therefore, a voltage applied on the electrodes generates an electric field over the optical guided mode, and this electric field is mainly horizontal and oriented along the Z-axis, as represented by the horizontal white arrows in **Figure 2(a)**.

r_{13} = 8.6 pm/V	r_{51} = 28 pm/V	r_{33} = 30.8 pm/V	r_{22} = 3.4 pm/V	n_o = 2.210	n_e = 2.138

n_e and n_o denote the extraordinary and ordinary index of the material.

Table 1. Electro-optical and optical properties of $LiNbO_3$ at 1550 nm wavelength [13].

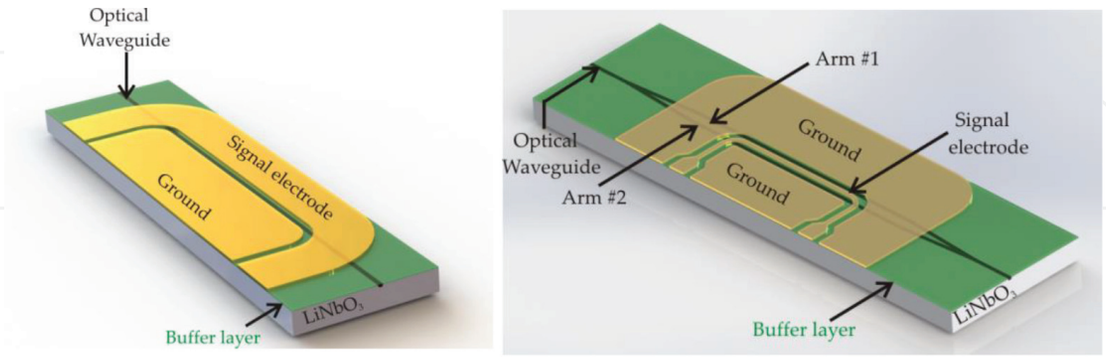

(a) (b)

Figure 1. Standard configurations of integrated $LiNbO_3$ optical modulators in a X-cut substrate. (a) Phase modulator. (b) Mach-Zehnder modulator with push-pull electrodes: The signal electrode is placed between the two arms of the integrated interferometer. The buffer klayer helps preventing from optical leakage in the electrodes, and it also helps to achieve index matching between the electrical and optical propagating waves.

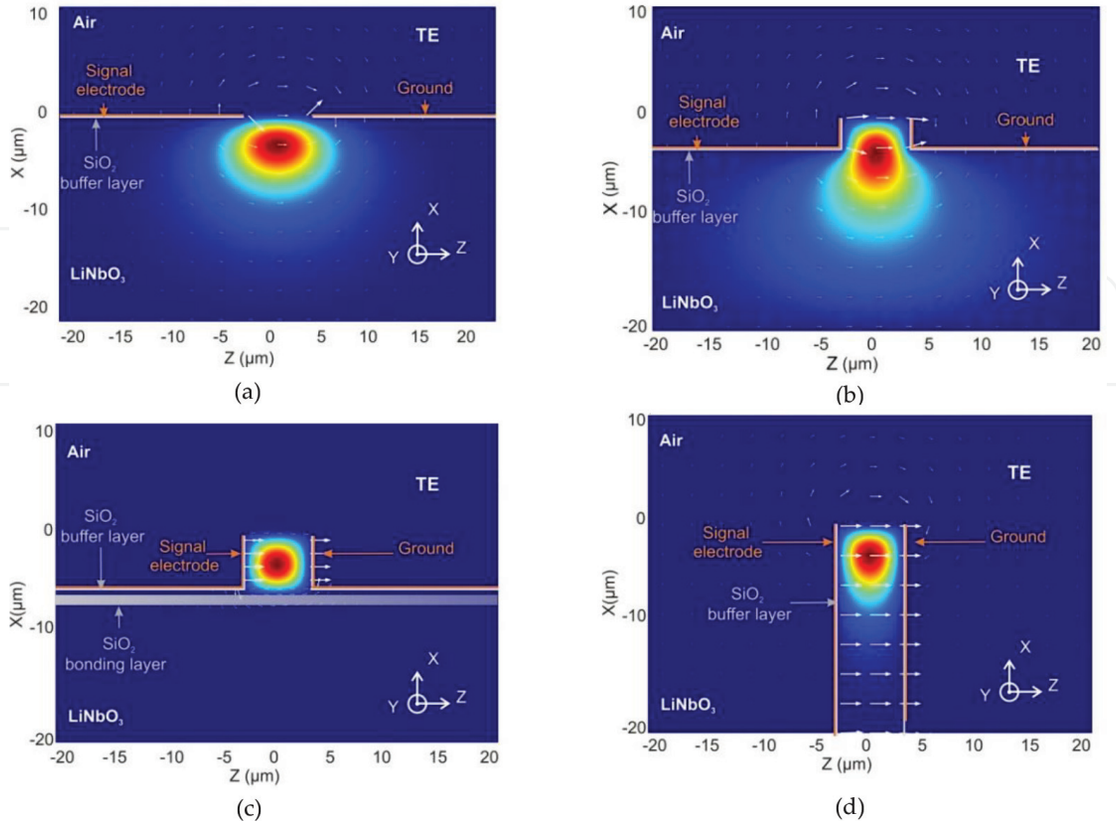

Figure 2. Cross-sections of optical waveguides. The electric optical guided mode and the applied electric field are calculated by F.E.M. (comsol® software) and represented with a color map and arrows respectively. (a) Standard Ti-indiffused waveguide with a gap g = 6 μm between electrodes, a thickness buffer layer t = 200 nm, and a w = 6 μm wide titanium rib. (b) Same waveguide as in (a), but with a ridge height h = 3 μm. (c) Adhered ridge waveguide with a width of 6 μm, a ridge height of 6 μm, a $LiNbO_3$ layer thickness of 6 μm; and t = 200 nm. (d) High aspect ratio ridge waveguide done by Ti-indiffusion. The ridge height is 19 μm and the width is 6 μm; t = 200 nm (a) Ti-indiffused waveguide, (b) standard ridge waveguide, (c) adhered ridge waveguide, (d) high-aspect ratio ridge waveguide.

In these conditions, the index modification induced by the voltage on the ordinary index and extraordinary index is evaluated through Eq. (2):

$$n'_o = n_o - \frac{n_o^3 \cdot r_{13} \cdot \Gamma \cdot V}{2 \cdot g} \text{ and } n'_e = n_e - \frac{n_e^3 \cdot r_{33} \cdot \Gamma \cdot V}{2 \cdot g} \tag{2}$$

where Γ is the electro-optic overlap coefficient that takes into account the non-uniform behavior of the electric field over the optical mode cross-section:

$$\Gamma = \frac{\iint \varepsilon_Z^2 \cdot E_3 \cdot dS}{\iint \varepsilon_Z^2 \cdot dS} \cdot \frac{g}{V} \tag{3}$$

ε_z denotes the third component of the electric optical field $\vec{\varepsilon}$ in the crystalline coordinate system, and E_3 is the electric field induced by the voltage V applied on the electrodes. So in

Configuration	Definition of the phase induced shift	Expression of V_π
Phase modulation **Figure 1(a)**	$\varphi = \frac{\pi \cdot V}{\lambda \cdot g}\left(\Gamma \cdot n_e^3 \cdot r_{33}\right)L$	$\frac{\lambda \cdot g}{\left(\Gamma \cdot n_e^3 \cdot r_{33}\right)L}$
Intensity modulation **Figure 1(b)**	$\Delta\varphi = \frac{2\pi}{\lambda}\frac{n_e^3 \cdot r_{33} \cdot V}{2 \cdot g}(\Gamma_1 - \Gamma_2)L$	$\frac{\lambda \cdot g}{n_e^3 \cdot r_{33} \cdot (\Gamma_1 - \Gamma_2)L}$

Γ_1 and Γ_2 denote the electro-optic overlap coefficients in arm #1 and arm#2 of the Mach-Zehnder device, respectively, when the polarization is parallel with (OZ). In a symmetric X-cut standard Mach-Zehnder configuration, $\Gamma_1 = -\Gamma_2$. Values of Γ are strongly dependent on the electrode and buffer layer thickness.

Table 2. Evaluation of the electro-optic efficiency in classic configurations.

other words, Γ is the average electric field seen by the optical electric field and normalized by V/g. Noteworthy, Γ can be larger than 1 in specific cases.

Two basic configurations can be distinguished, the first one being the phase modulator for which only the phase of the optical signal is modified by the electric field (see **Figure 1(a)**) and the second one being the intensity modulator which exploits the interference between two signals having different paths in the material, such as the Mach-Zehnder illustrated schematically in **Figure 1(b)**. A precise evaluation of the electro-optic efficiency is given by the half-wave voltage, which is the voltage needed to obtain an induced phase shift of π. In the case of a phase modulator, the phase shift φ denotes the phase accumulated through the electrode length L, and its expression is summarized in row #1 of **Table 2**. In a Mach-Zehnder intensity modulator, the phase shift $\Delta\varphi$ corresponds to the phase difference induced between the two arms at their output (see row #2 of **Table 2**).

From **Table 2** we can infer that the critical parameters for obtaining a low driving voltage V_π and therefore low power consumption are the gap g, the active length L, and the electro-optic overlap coefficient Γ. In standard modulators, g ranges from 6 to 30 μm, depending on the targeted performances in terms of impedance, bandwidth, and voltage, and Γ is usually lower than 0.5, which is due to the weak overlap between the electrical field and optical guided mode. As an example, Γ = 32% in the X-cut Ti-indiffused phase modulator with g = 6 μm and with a δ = 0.2 μm silica buffer layer thickness calculated in **Figure 4(a)**. This means that an electrode longer than L = 2 cm is needed to obtain a driving voltage lower than 5 V. So the achievement of compact modulators with low driving voltage requires an increase of Γ.

This latter is controlled by the fabrication technologies enabling more or less tight light confinement. In the following paragraphs we describe the evolutions from the first $LiNbO_3$ guides to the recent confined ones with increased Γ.

3. Standard waveguides

Titanium diffusion and proton exchange (PE) constitute the two main commercial techniques for the manufacture of $LiNbO_3$-based optical waveguides.

3.1. Titanium-indiffused waveguides

Since their discovery in 1974 by Schmidt et al. [14], Ti-indiffused optical waveguides have maintained continuous interest for commercial applications in high-bit-rate data-processing systems. More recently, they have attracted attention for mid-infrared applications dedicated to astrophysics [11, 15] or spectrometry [16].

Titanium-indiffused waveguides are fabricated through the diffusion of titanium ribs at a high temperature (~1000°C). The typical width of the Ti ribs is 6–7 μm and the thickness ranges from 80 to 100 nm for operations at 1550 nm wavelength. Extensive description of the process is given by Burns et al. [17]. Ti-indiffused waveguides have the advantages of low insertion losses (1 dB by Ramaswamy [18]). Their ability to guide two polarizations is also a specificity of interest, and they are good candidates over a very large spectral bandwidth from 1.0 to 4.7 μm.

The particularity of Ti-indiffused waveguides is their weak light confinement. Typically, the full width at half maximum (FWHM) of a standard X-cut Ti-indiffused waveguide working at 1550 nm is 7.5 μm in the horizontal direction and 4.8 μm in the vertical direction. This specificity allows a large η overlap integral with single-mode fibers (SMF), expressed by Eq. (4):

$$\eta = \frac{\iint_S \varepsilon_{fiber}(x,z)\cdot\varepsilon^*_{guide}(x,z)\cdot dS}{\left(\iint_S \varepsilon_{fiber}(x,z)\cdot\varepsilon^*_{fiber}(x,z)\cdot dS\right)\left(\iint_S \varepsilon_{guide}(x,z)\cdot\varepsilon^*_{guide}(x,z)\cdot dS\right)} \tag{4}$$

where $E_{fiber}(x,z)$ denotes the spatial distribution of the optical guided electric field within the fiber, and $E_{guide}(x,z)$ is the spatial distribution of the optical guided electric field within the optical waveguide. η can be larger than 85% in Ti-indiffused waveguides, which explains their low coupling losses with fibers and consequently their low insertion losses.

Although attractive for obtaining low losses, the weak light confinement is limiting for EO interaction, which is illustrated by a small Γ of 32% in the example of **Figure 2(a)**. Therefore, Ti-indiffused waveguides are not the best candidates when compact and efficient EO modulators are required and alternative techniques have been considered.

3.2. Proton exchange-based waveguides

Proton exchange guides are well appreciated for non-linear periodically poled $LiNbO_3$ devices [19], due notably to a photorefractive threshold higher than Ti-indiffused waveguides [20]. The polarizing nature of PE waveguides also makes them prime waveguides for applications where polarization control is crucial. Fiber-optics gyroscopes [21] and polarizing phase modulators are particularly concerned [10].

Proton exchange [22] is a low-temperature process ($\sim$ 120–250°C) whereby Li ions from the $LiNbO_3$ wafer are exchanged with protons from an acid bath. Exchanged layers exhibit an increase in the extraordinary index and a slight decrease in the ordinary index, which is the origin of the polarizing nature of the PE-based waveguides. In the most general case, the

proton exchange zones may consist of several phase multilayers, which deteriorate their electro-optical performance. Several techniques have been successfully developed to design the index profile and to restitute the phase and optical properties. The mostly used techniques are:

- Annealed-PE [23], where annealing is performed subsequently to PE for obtaining mono-phase waveguides with restored EO properties;
- Soft-PE [24], where the proton exchange is done in soft conditions in buffered melts (i.e., lithium benzoate added to the benzoic acid) so that the optimal mono-phase waveguides are obtained in a one-step process;
- Reversed-PE, where the PE waveguides are immersed in a eutectic mixture of $LiNO_3$, KNO_3, and $NaNO_3$ to achieve buried waveguides with minimal loss connections with optical fibers.

Similar to Ti-indiffused waveguides, PE-based waveguides can yield very low insertion losses [25]. If light confinement is slightly tighter than their Ti-indiffused counterparts, PE-based waveguides are however not confined enough to reduce significantly the active length of EO modulators.

This observation led to strong efforts in the 1980s to obtain waveguides with both tight light confinement and low insertion losses. The first proposed solutions were based on ridge waveguides.

4. Ridge waveguides

As represented in **Figure 2(b)–(d)**, a ridge waveguide is an optical waveguide etched on both sides: the lateral confinement is ensured by a step index between $LiNbO_3$ and air. This configuration was firstly proposed by Kaminow et al. more than 40 years ago [26] to achieve a lateral confinement in planar Ti-outdiffused waveguides. Ridge waveguides are still a hot topic in research, with applications and manufacturing techniques evolving over the years.

4.1. Ridge made in standard waveguides by wet etching or plasma etching

The first generation of ridge waveguides was produced through Ti indiffusion or proton exchange techniques followed by dry or wet etching. The wafer thickness was about 500 μm and the ridge depth was typically lower than 10 μm. If their first apparition was in 1974, their attractiveness dates from the mid-1990s, when ridges were identified as the best solution to achieve both large bandwidth and impedance matching in EO Mach-Zehnder interferometers for long-haul high-bit-rate telecommunication systems [27]. Noteworthy, the moderate depth of the ridges was compatible with standard metal deposition techniques, which was convenient for the electrode deposition. Hence, ridge-based modulators with bandwidth as high as 100 GHz and driving voltage of 5.1 V were demonstrated [28] with 2-cm-long electrodes in

Mach-Zehnder modulators. The reported ridges were achieved through Ti indiffusion followed by selective dry etching with electron cyclotron resonance with argon and C_2F_6 gases.

More generally, most of the reported dry etching techniques use fluorine-based gases to exploit their chemical reactivity with $LiNbO_3$. Wet etching techniques associated with ion implantation, proton exchange, or domain inversion have also been widely studied [29, 30]. When followed by a subsequent step of annealing or Ti-in-diffusion at high temperature, the method is very efficient for the fabrication of ultra-smooth ridges with propagation losses as low as 0.05 dB/cm [31].

However, the etching step lasts for several hours to obtain depths of a few micrometers, and such small depths do not increase the EO efficiency significantly as compared with a standard waveguide. This is illustrated in **Figure 2(a)** and **(b)** where the increase of Γ is only 18% in the 3-μm-deep ridge, as compared with the Ti-indiffused waveguide. According to finite element method (FEM) calculations, the ridge depth needs to be higher than 8 μm (see **Figure 2(d)**) or the substrate needs to be thinned down to a few micrometers (see **Figure 2(c)**) to achieve an increase larger than 60% in EO efficiency. Therefore, alternative techniques have been proposed, based on mechanical machining, to produce more efficient ridges.

4.2. Adhered ridge waveguides

Adhered ridge waveguides are made through mechanical processing. In a first step, the $LiNbO_3$ wafer is bonded to another one ($LiNbO_3$, $LaTiO_3$, Si…), and then the wafer is thinned down to a few micrometers by lapping polishing. Finally grooves are inscribed inside the thinned wafer by precise dicing [32] or by dry etching [33]. The adhered ridge waveguide is the remaining matter between two grooves. The first adhered ridge waveguide [32] aimed at replacing PE-based waveguides whose mobile protons induce long-term degradation of the optical response. The main application was nonlinear frequency conversion.

Since then, adhered ridge waveguides have been widely employed still for nonlinear (NL) applications [34, 35]. The typical thickness of the $LiNbO_3$ thinned layer ranges from 3 to 10 μm; the width of the ridge is typically 3–5 μm, and the depth is usually lower than the $LiNbO_3$ layer thickness (see **Figure 2(c)**). The pigtailing is performed by using lens coupling and laser welding [34]. Such pigtailed modules are now commercialized [36].

As attractive as they may be for NL applications, adhered ridge waveguides do not attract much attention for electro-optical modulation. One of the reasons is their multimode behavior which limits the modulation contrast. A step has been put forward with high-aspect ratio ridge waveguides having spot-size-converters, allowing for low insertion losses and for the filtering of optical modes.

4.3. High-aspect ratio ridge waveguides made by optical grade dicing

High-aspect ratio (HAR) ridge waveguides are ridges with depths larger than 10 μm (see **Figure 2(d)** and **3**). Such depths are achieved by optical grade dicing, meaning that the substrate is diced and polished at the same time [37]. In a first step, optical channels or planar

http://dx.doi.org/10.5772/intechopen.76798

waveguides are made simply through standard techniques (Ti indiffusion, proton exchange, ion implantation), and in a second step two grooves are diced along waveguide sides. If the machining parameters—such as translation and rotation speeds and nature and size of the blade—are properly chosen, the ridge patterns are diced and polished at the same time, which yield roughness lower than 20 nm and propagation losses lower than 0.1 dB/cm [37]. The resulting depths can be higher than 500 (see **Figure 3(a)**), but the preferred depth is between 10 and 50 μm [38] to obtain robust reproducible guided mode cross-sections that are independent on the ridge depth.

The uniform deposition of a buffer layer over the vertical edges of the ridge can be accomplished by atomic layer deposition (ALD), followed by a two-step side deposition of electrodes [39]. A schematic overview of the resulting EO ridge is seen in **Figure 4(a)**, while **Figure 4(b)** shows a standard electron microscope (SEM) image of the EO HAR ridge with ALD-deposited buffer layer.

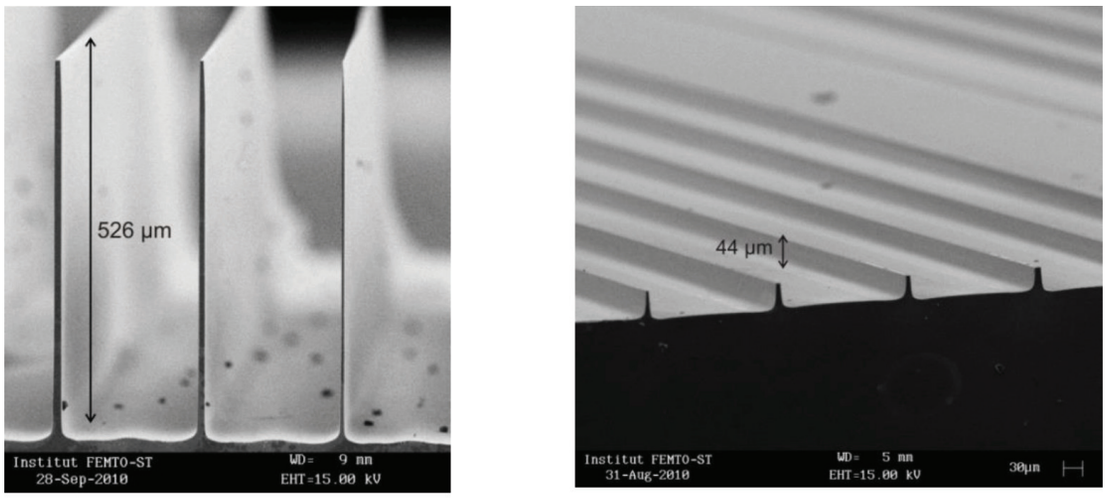

(a) (b)

Figure 3. SEM images of high aspect ratio ridge waveguides. Record aspect ratio with a depth of 526 μm for a width of only 1 μm. (b) Optimal high aspect ratio waveguide, in term of robustness and losses [38].

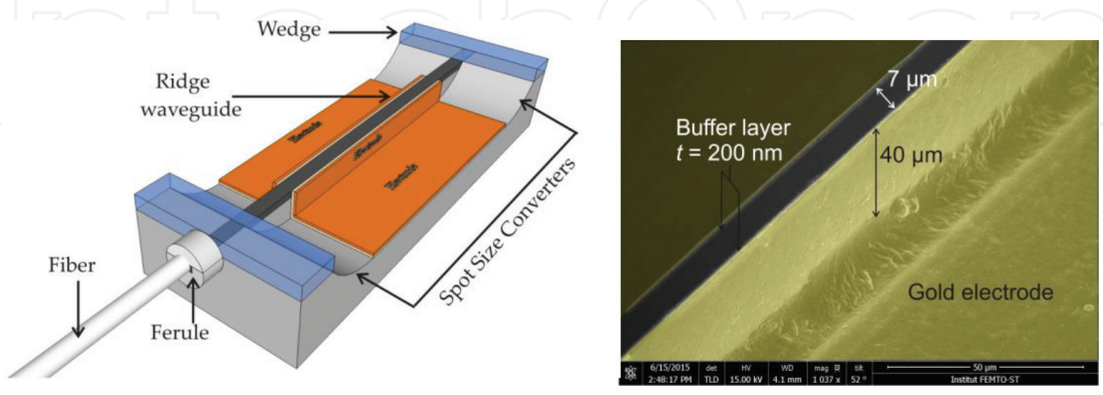

(a) (b)

Figure 4. Ridge-based EO device. (a) Electro-optical ridge buffer layer with electrodes and spot-size-converters. (b) SEM image of an EO ridge with vertical buffer layer and electrodes.

Finite element method (FEM) simulations performed on HAR waveguides show that they are optimal in terms of EO efficiency, since the electric field is uniform over the optical waveguide. This is illustrated in **Figure 3(d)** with the white arrows representing the applied electric field. As a consequence, the electro-optical coefficient can be evaluated simply as a function of g:

$$\Gamma = \frac{g \cdot \varepsilon_{diel}}{2 \cdot \varepsilon_{LN} \cdot \delta + (g - 2 \cdot \delta) \cdot \varepsilon_{diel}} \tag{5}$$

where δ denotes the buffer layer thickness and ε_{LN} and ε_{diel} are the dielectric permittivities of $LiNbO_3$ and of the buffer layer, respectively. A quantitative comparison between a HAR ridge waveguide and a standard Ti-indiffused waveguide with the same gap and the same buffer layer shows that Γ is increased twofold in favor of the HAR ridge waveguide. This was confirmed experimentally by Caspar et al. [39].

However, the counterpart of the strong lateral confinement is a weaker mode matching with SMFs: the η coefficient is reduced down to 50%, meaning that 50% of the optical energy is lost per facet and consequently the insertion losses are ineluctably higher than 6 dB. This issue can be circumvented by using vertical spot-size converters such as the ones schematically depicted in **Figure 4(a)**. They are made simply by progressively decreasing the ridge depth, which can be done by lifting the blade before the end of the ridge. In this case, the total insertion losses are measured to be lower than 3 dB for a 2-cm-long ridge, and only the fundamental mode is allowed to propagate in the ridge [40].

If the high-aspect ratio ridge waveguide is the best configuration in terms of EO efficiency, there is however an interest in developing confined waveguides allowing more complex patterns than straight waveguides. This is the reason why thin films and membranes have also known to be a great success over the years.

5. Thin film-based and membrane-based waveguides

Thin film-based waveguides can be described as rib waveguides or gradient index-based waveguides integrated in $LiNbO_3$ thin films with a thickness lower than 5 mm. Ion slicing [41] is currently the prevailing manufacturing technique. These waveguides are also called microwaveguides.

5.1. Thin films fabricated by ion slicing

By combining wafer bonding and ion implantation, the ion slicing technique allows the wafer-scale production of thin layers of Z-cut and X-cut substrates with sub-micrometric thickness, and the roughness is lower than 0.5 nm [42]. More precisely, the fabrication process begins by He^+ ion implantation with a dose of about 4×10^{16} ions/cm^2 to form an amorphous layer at a depth dependent on the implantation energy (typically a few hundreds of keV for submicronic $LiNbO_3$ layers). Then the implanted wafer is bonded to another one by using an intermediate layer with low refractive index, such as benzocyclobutene (BCB) or SiO_2 [42]. A thermal

treatment with temperature ramp is employed to split the samples along the implanted He layer. Hence, a thin $LiNbO_3$ layer bonded on another substrate remains. Afterward, annealing and chemical mechanical polishing are used to obtain a roughness of 0.5 nm. The technique is well mastered and thin-film $LiNbO_3$ layers are now commercialized [43, 44], which have boosted the development of compact $LiNbO_3$ components from low-loss ridge waveguides [45] to electro-optic microring resonators [46, 47], wire waveguide-based modulators [48], and nonlinear nanowires or ridges [49]. The lateral confinement can be ensured by proton exchange-based techniques or by direct etching of the thin layer. However, the insertion losses are often higher than 10 dB due to mode mismatch between the confined waveguides and the single mode fibers (SMFs) (see **Figure 5(b)**: the vertical confinement is significantly tighter than a standard SMF fiber, which leads to η coefficient lower than 10%).

One approach to reduce the coupling losses is to guide the light in another material than $LiNbO_3$. As an example, as studied by Chen et al. [50], the light is guided in a silicon-on-insulator microring bonded to an ion-sliced $LiNbO_3$ film. The resulting low insertion losses (4.3 dB) are mitigated by a figure of merit of $V_\pi \cdot L$ = 9.1 V·cm, which is no better than what is reported in standard Ti-indiffused waveguides. The compacity is however made possible by using a microring resonator with small radius curvature and low radiation losses.

Another approach has been proposed recently, which relies on an easy-to-implement technique and allows low-loss free-suspended waveguides with calibrated thickness.

5.2. Suspended membranes fabricated by optical grade dicing

Figure 6 shows how free-suspended waveguides can be made by optical grade dicing. A monomode optical waveguide is firstly fabricated through the diffusion of 6-μm-wide and 90 nm-thick Ti stripes at 1030°C for 10 h. Then, gold electrodes are sputtered over the substrate. Noteworthy, the electro-optical patterns are achieved by UV lithography, so that many other patterns can be envisioned with the same technology. Then, a curved slot is inscribed into

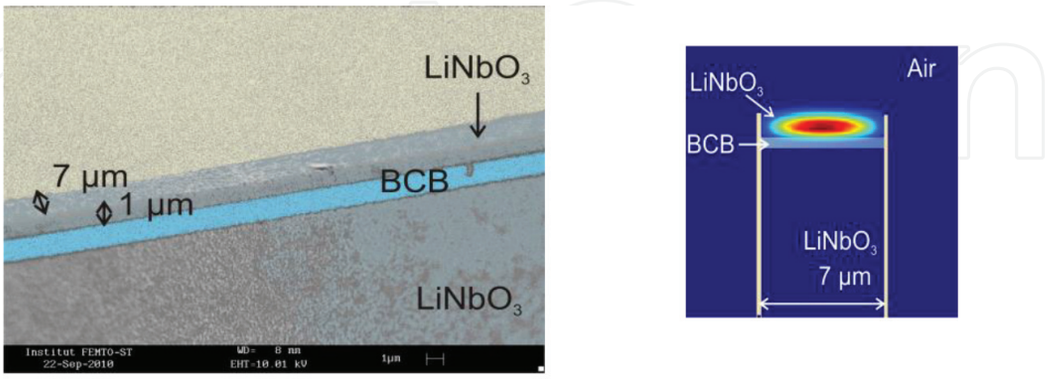

(a) (b)

Figure 5. Thin film-based wire waveguides. (a) SEM image of a wire waveguide made by ion slicing. The dielectric bond layer is a BCB. (b) Amplitude of the electric field, TE optical mode calculated F.E.M. The overlap coefficient with a SMF mode is lower than – 10 dB.

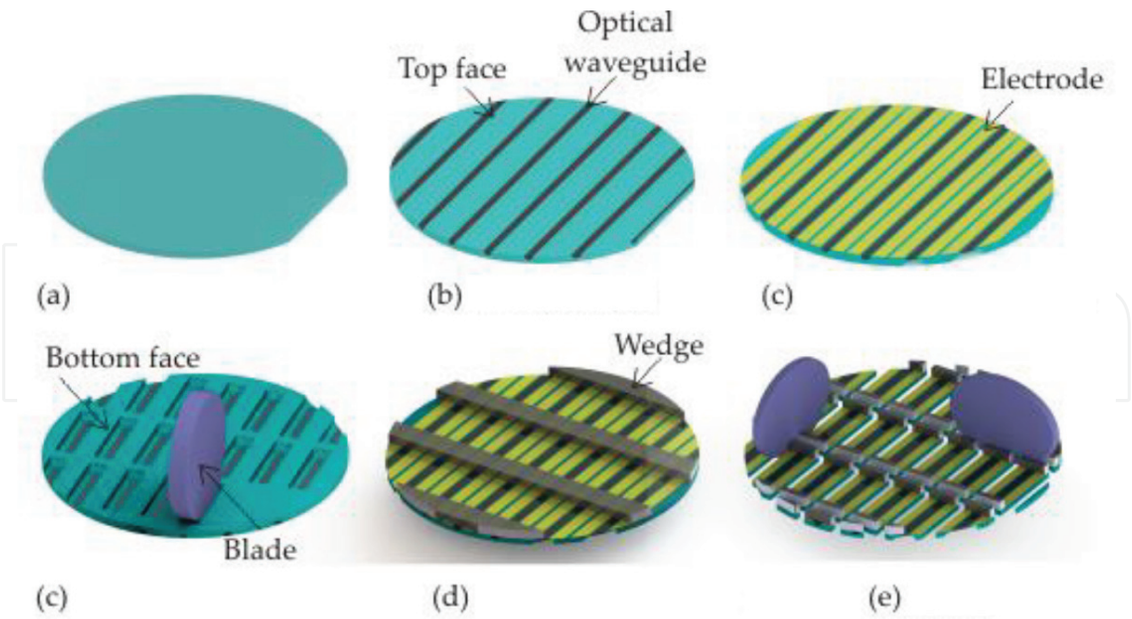

Figure 6. Process flow for the production of low-loss free-standing electro-photonic waveguides. The bottom face is the face of the wafer opposite to the waveguides.

the bottom face as schematically depicted in **Figure 6(c)** by optical grade dicing. The rotation speed and the moving speed of the 3350 DISCO DAD dicing saw are, respectively, 10,000 rpm and 0.2 mm/s. A resinoid blade progressively enters the wafers to a depth δ_b and inscribes a curved shape inside the bottom face of the sample. Then, the blade is translated along the waveguide and it is lifted before the end of the waveguide. The remaining matter is a membrane with a controlled thickness $t = e\text{-}\delta_b$ where e is the wafer thickness. Thanks to this technique, vertical tapers are fabricated at the extremities of the membrane [51]. Indeed, they are created by the curved shape of the blade (see **Figure 6** and the tapers in **Figure 7**). Finally, wedges are bonded by UV adhesive on the top face of the wafer, and the chips are separated by optical grade dicing, enabling polished facets with an enlarged surface for pigtailing with fibers.

Figure 7 shows a schematic diagram of a resulting membrane-based electro-optical waveguide. In the free-standing Section 1, the waveguide is thinned, and the thickness can take any value between 450 nm and 500 μm. This is achieved by a preliminar depth calibration in a dead zone of the wafer. The suspended waveguide is surrounded by electrodes allowing an electrical control of the effective refractive index. The cross-sections in **Figure 7** represent the optical guided mode along the suspended waveguide. In Section 1, the strongly confined mode allows an electro-optical coefficient twofold higher than in Section 3. On the other hand, the weakly confined mode in Section 3 allows mode matching and low coupling losses between the waveguide and the SMFs. Hence, the overlap coefficient η can be as high as 85%. Additionally, to mode matching with fibers, the vertical tapers allow filtering in favor of the fundamental mode, which avoids parasitical beatings in the spectral transmission response [51].

The experimental measurements of losses are summarized in **Table 3** for both TE and TM polarizations and for different thicknesses. They are also reported by Courjal et al. [51]. They are compared with the average propagation losses of a non-thinned Ti-indiffused waveguide (t = 500 μm) fabricated in the same conditions with the same total length. The measurements

http://dx.doi.org/10.5772/intechopen.76798

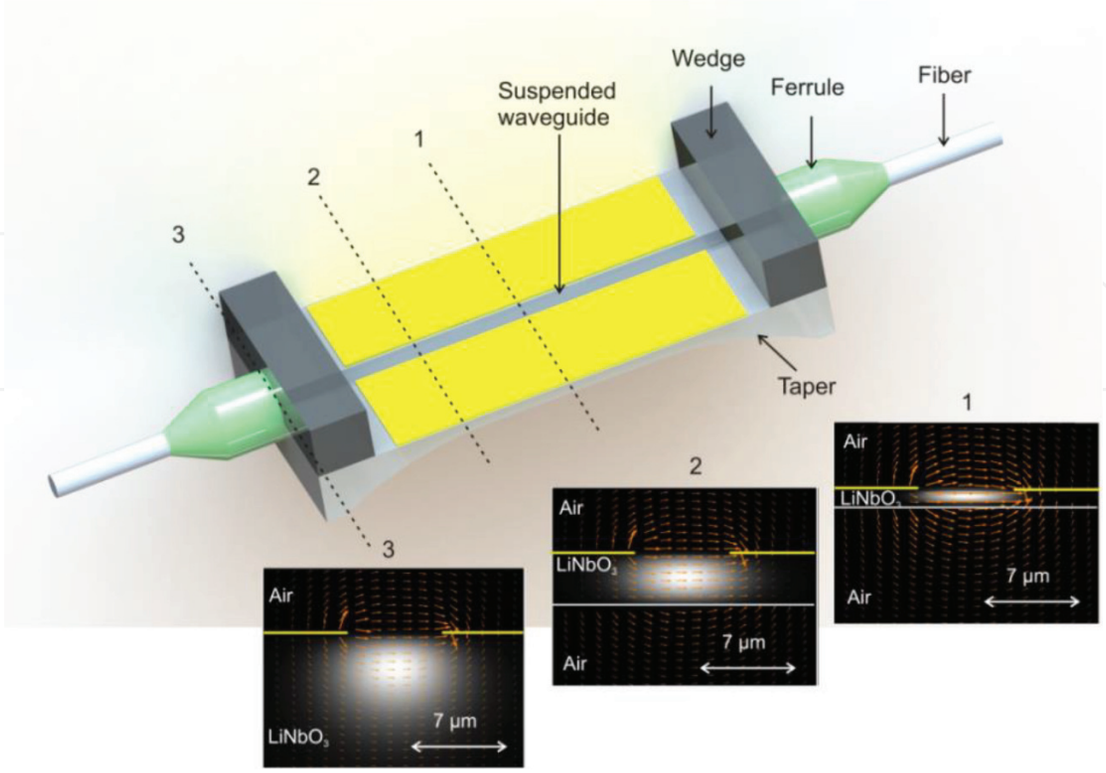

Figure 7. Schematic diagram of a free-suspended waveguide made by optical-grade-diving. The waveguide is thinned locally to get high EO efficiency. It is surrounded with tapers allowing mode matching. The inserts show the optical guided mode in different sections. Section#1: The layer thickness is 1 μm. Section#2: The layer thickness is 4 μm. Section#3: The layer thickness is 500 μm.

T (μm)	Pol.	α (dB/cm)	Total IL (dB)	ξ (dB)	$\Delta n_g/\Delta V$ (R.I.U./V)	Γ (%)
7500	TE	0.20 ± 0.06	2.8 ± 0.2	1.1 ± 0.3	$7.8 \pm 1.0.10^{-6}$	34
	TM	0.22 ± 0.06	2.8 ± 0.2	1.1 ± 0.3	$3.2 \pm 1.0{\cdot}10^{-6}$	35
4.50	TE	0.20 ± 0.06	2.8 ± 0.2	1.1 ± 0.3	$13.4 \pm 1{\cdot}10^{-6}$	58
	TM	0.32 ± 0.06	2.9 ± 0.2	1.1 ± 0.3	$15.8 \pm 1{\cdot}10^{-6}$	175
0.45	TE	3.20 ± 0.06	6.6 ± 0.5	1.1 ± 0.3	—	—
	TM	5.12 ± 0.06	8.1 ± 0.8	1.1 ± 0.3	—	—

t, α, IL,ξ are respectively the membrane thickness, the average propagation losses, the insertion losses, the reflection coefficient and the coupling losses per facet. Γ is the overlap coefficient deduced from the measured $\Delta n_g/\Delta V$. The 450 nm-thick waveguides did not have electrodes so that the EO measurements could not be performed.

Table 3. Experimental assessment of losses for X-cut membrane-based waveguides with a total length of L = 1.1 cm at 1550 nm wavelength.

were repeated five times for each waveguide and polarization. When the membrane has a thickness $t \geq 7$ μm, there is no difference observed between a membrane-based waveguide and non-thinned one. When the waveguide is thinned below 4.5 μm, the guided wave undergoes increased propagation losses, up to 5.1 dB/cm for the TM wave and 3.2 dB/cm for the TE wave when t = 450 nm. Overall, the losses are lower for the TE waves than for TM waves, which is

due to an increased sensitivity of the TM waves to membrane roughness. It is noteworthy that the coupling losses remain the same regardless of the membrane thickness, which confirms the efficiency of the tapers to mode match with the fibers.

The EO overlap coefficient is deduced from the Fourier transform of the reflected spectral density (see **Figure 8**), which is also the autocorrelation of the impulse response. Due to the Fabry-Perot oscillations inside the cavity formed by the waveguide, a peak appears in the Fourier transform, which coincides with a round trip of the light between the two facets of the waveguide. From this peak, we can deduce the global effective group index: $n_{geff} = t_2 \cdot c_0/(2 \cdot L_{tot})$, c_0 being the speed of light and L_{tot} denoting the waveguide length. The resulting effective group indexes are $n_{effTE} = 2.189 \pm 0.005$ and $n_{effTM} = 2.269 \pm 0.005$ for TE and TM polarizations, respectively, in an X-cut Y-propagating waveguide with a membrane thickness of 4.5 μm. The effective group index is measured voltage by voltage from **Figure 8**, for the assessment of the group index variation per voltage: $\Delta n_g/\Delta V$. The results are exposed in **Table 2**. Γ is calculated from $\Delta n_g/\Delta V$ by using expressions (6) and (7) for the TE and TM waves, respectively:

$$\Gamma_{TE} = \frac{\Delta n_{eg}}{\Delta V} \cdot \frac{2 \cdot g}{n_e^3 \cdot r_{33}} \tag{6}$$

$$\Gamma_{TM} = \frac{\Delta n_{og}}{\Delta V} \cdot \frac{2 \cdot g}{n_o^3 \cdot r_{13}} \tag{7}$$

Table 2 confirms the twofold enhancement of the EO interaction when the membrane is thinned down to 4.5 μm, and it shows that this enhancement is even higher for the TM-propagating wave, although this was not anticipated from the FEM calculations. This latter result can be of great interest to seek for isotropic EO behavior of the guided wave in the presence of an applied voltage.

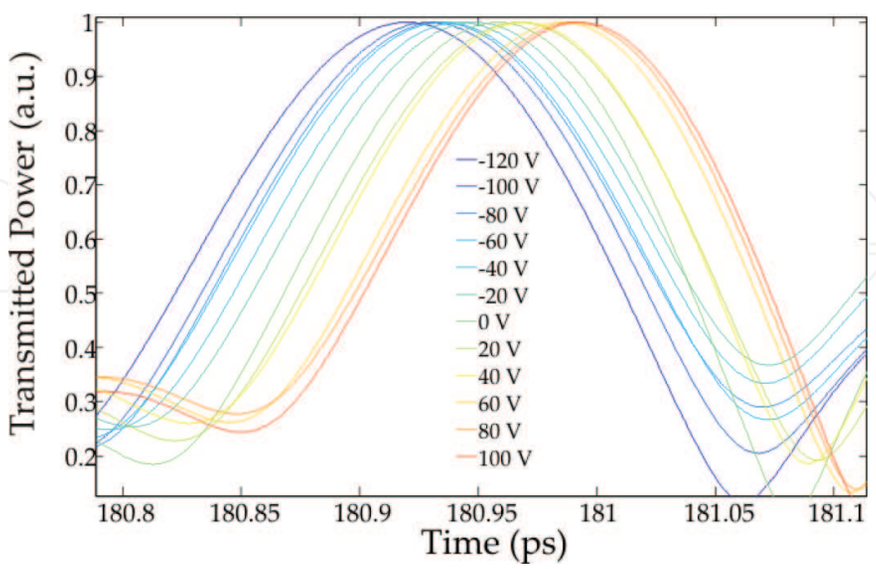

Figure 8. Zoom view of the Fourier transform of the reflected optical density spectrum. These measurements are achieved as a function of the applied voltage through a 12.0 mm long tapered-membrane-based waveguide with a width of 6 μm and a thickness of 4.5 μm. The total length was L_{tot} = 1.2 mm.

http://dx.doi.org/10.5772/intechopen.76798

So membrane-based waveguides are good candidates to reduce the active length, without impacting the other parameters such as the losses. It is now tempting to go one step further toward compacity by inscribing nanostructures inside the membranes.

6. $LiNbO_3$ nanostructures and photonic crystals

It is well established that the machining of materials at the wavelength scale can yield a specific control of the light flux, which is of great interest to enhance significantly the electro-optical efficiency. In particular, photonic crystals (PhCs) are periodic structures that are designed to affect the motion of photons in a similar way that periodicity of a semiconductor crystal affects the behavior of electrons. The non-existence of propagating electromagnetic modes inside the structures at certain frequencies introduces unique optical phenomena such as tight light confinement. The part of the spectrum for which wave propagation is not possible is called the photonic bandgap (PBG).

The first reported PhC-based EO $LiNbO_3$ modulator [52] was configured to behave as an electro-absorbent modulator: it was designed to have a photonic bandgap, and the spectral edge was exploited for intensity modulation. Hence, an active length of 11 μm was sufficient to modulate the light with a driving voltage of 13 V [52]. A schematic diagram of such a device is seen in **Figure 9**. It consists of a square lattice PhC integrated on an annealed proton exchanged optical waveguide and surrounded by capacitive coplanar electrodes. The $LiNbO_3$ PhC was fabricated through focused ion beam (FIB) milling The refractive index was modified by the electric field *Ez* generated between the electrodes, which moved the spectral position of the PBG and consequently the transmitted intensity. The geometric properties of the PhC were chosen to benefit from slow light effects.

This compact modulator showed an EO interaction 312 times higher than the one predicted from Eq. (2): the extraordinary effect is shown in **Figure 10** where the PBG is spectrally shifted

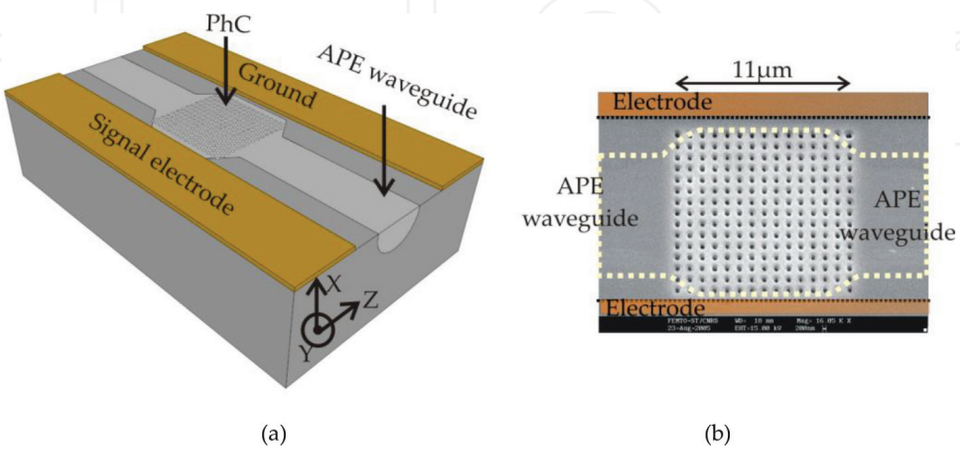

Figure 9. Image of the first reported PhC-based EO modulator [53]. (a) Schematic view of the ultra-compact modulator. (b) SEM image of the photonic crystal surrounded by electrodes.

by 100 nm when only 40 V is applied on the electrodes. This effect is attributed to an enhanced field factor *f* induced by slow light effect:

$$\mathrm{f} = \sqrt{\frac{v_g^{BULK}}{v_g^{PC}}} \tag{8}$$

where v_g^{BULK} is the group velocity in the bulk material and v_g^{PC} is the group velocity in the photonic crystal. The EO enhancement is explained by Roussey et al. [53] by an effective EO coefficient being enhanced by the local field factor as follows:

$$r_{33}^{PC} = f^3 r_{33} \tag{9}$$

The local field factor was calculated by using the slope of the band dispersion diagram and was evaluated to be 6.8 which was in good agreement with the measurements. To our knowledge, this huge effect is still a record in terms of EO sensitivity. However, as performing and attractive as this configuration may appear, the transmission losses were of 10 dB (see **Figure 10(a)**), which is prohibitive for commercial applications. The small extinction ratio (12 dB) was also limiting for many demanding EO applications. These limitations are mainly due to the weak light confinement inside the APE waveguide, combined with the conical shape of photonic crystals that provoked deviation of light inside the substrate [54].

Since then, other approaches have been proposed, based on microring resonators or PhCs in thin films, enabling low propagation losses and high extinction ratio [42]. However, as mentioned in Section 5.1, these techniques are prohibitive in terms of fiber coupling, due to the mode mismatch between the fiber and the guided mode inside the thin film, which also induces insertion losses larger than 10 dB.

In this context, the suspended waveguides mentioned in Section 5.2 appear as good candidates for hosting photonic crystal and nanostructures. There are not many publications on the

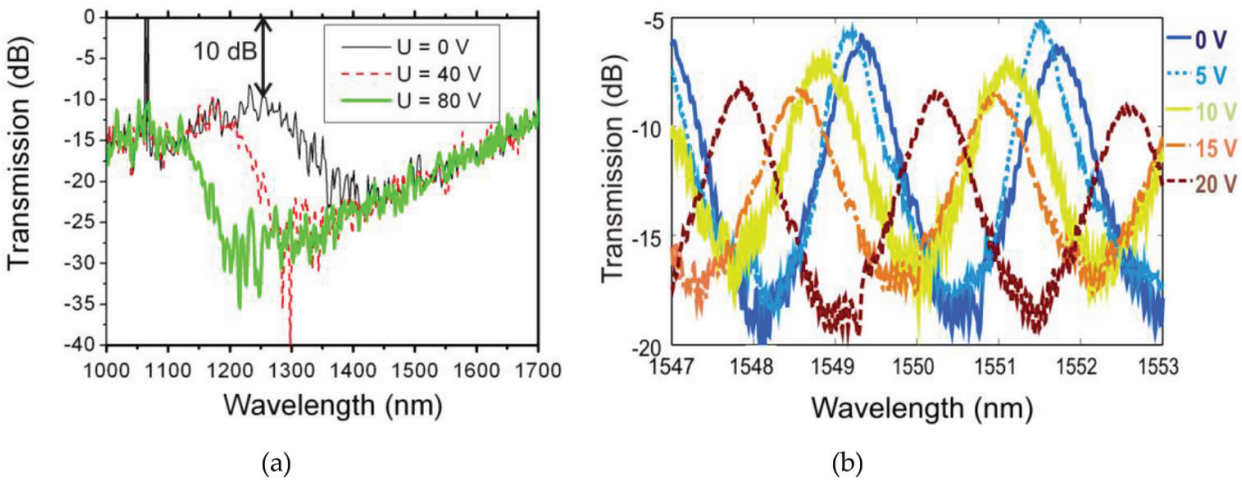

Figure 10. Spectral transmission responses through two PhC-based EO $LiNbO_3$ modulators, TE polarization. (a) Normalized transmission response through the modulator seen in **Figure 11**. (b) Normalized transmission response through a suspended Fabry-Perot [Caspar16]. The two measurements are done by direct butt-coupling with SMFs.

http://dx.doi.org/10.5772/intechopen.76798

subject yet, but the inscription of a 1D-PhC cavity as reported by Courjal et al. [51] appears like a good start. The component is made of two 1D PhCs separated by 200 μm in a free-suspended membrane. The 1D PhCs are designed to be reflectors at 1550 nm wavelength and their pair constitutes a Fabry-Perot cavity. One of them can be visualized in **Figure 12(b)**. The free spectral range of 2.7 nm seen in **Figure 10(b)** is in good agreement with the theoretical prediction: FSR=$\lambda^2/(2\cdot\Delta\cdot n)$, where Δ is the distance between the two 1D PhCs. The quality factor is measured to be of 2580, revealing moderated reflectivity of the 1D PhC ($R \approx 50\%$). The spectral position of a resonance peak shown in **Figure 10(b)** is shifted by 40.0 pm/V, which is not as high as the shift reported in **Figure 10(a)**, but this is balanced with the transmission losses that are diminished by 5 dB.

The driving voltage is assessed by measuring the output optical power at 1550 nm. The measured electro-optical response reported in **Figure 11** shows a 9.6 V driving voltage for the TE-polarized wave and 25.2 V for the TM-polarized wave. So the figure of merit for each polarization is, respectively, 1.9 and 5 mV·m, for TE and TM waves, which is 40-fold higher than the ones classically measured in Mach-Zehnder intensity modulators. In the compact modulator of **Figure 9**, the EO interaction was enhanced by means of slow light effects. Here the remarkable EO sensitivity is rather attributed to a tip effect that enhances the electric field in the vicinity of the Bragg grating.

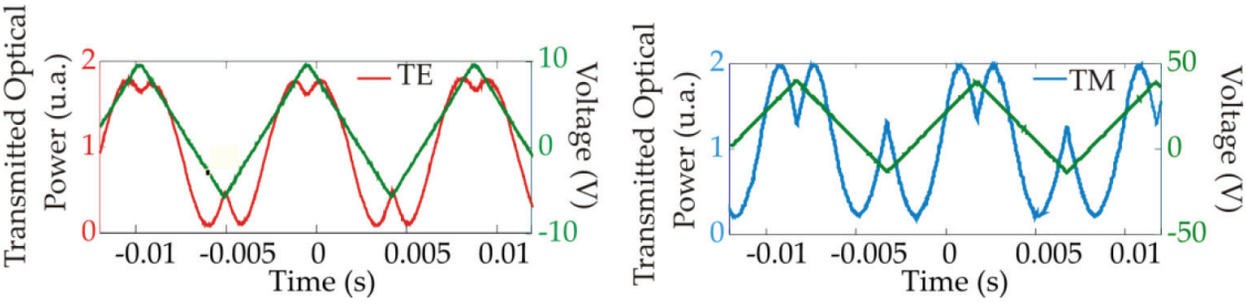

Figure 11. Experimental EO response of a TE wave (a) and TM wave (b) at the output of a 200 μm-long Fabry-Perot integrated in a 4.5 μm thick membrane.

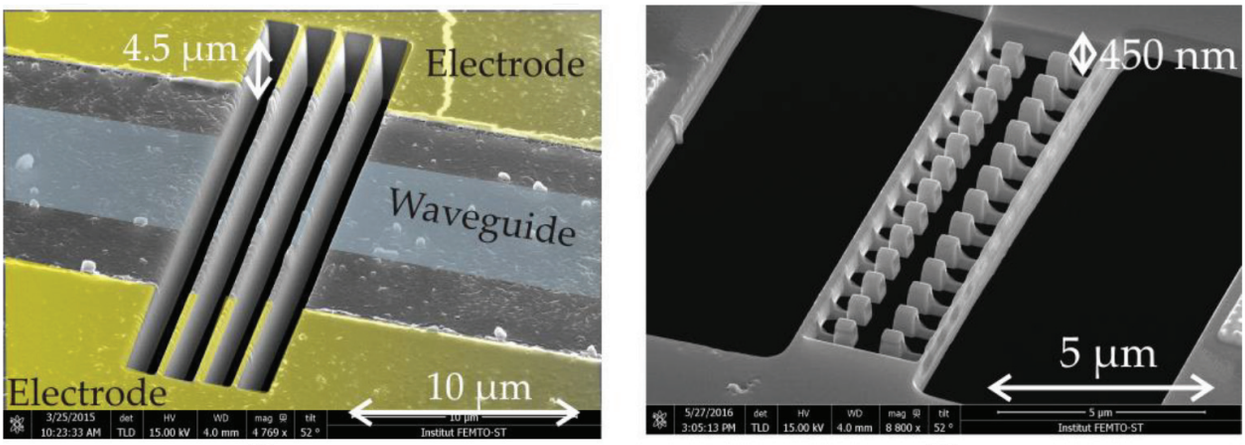

(a) (b)

Figure 12. SEM views of $LiNbO_3$ free-suspended membranes done by optical-grade dicing. The patterns are inscribed by FIB milling. (a) 1D-PhC implemented in a 4.5 μm-thick waveguide. (b) Nanostructure in a 450 nm thick membrane. Such a thickness is a record for a free-suspended layer fabricated through mechanical approach.

So, PhC-based EO modulators are extremely promising for the achievement of low-power consuming and compact modulators either by exploiting slow light effects in the nanostructure or tip effects in structured electrodes. The recent developments reported on free-suspended membranes appear to be also very promising for preserving low losses. The achievement of commercial performances should be achieved by a better control in fabrication of the 1D PhCs.

Many other 2D suspended devices may be envisioned by using the same technique: as a perspective, **Figure 12** shows SEM images of diced membranes hosting micro- and nano-patterns that can be used as $LiNbO_3$ MEMs, opto-mechanical, or nonlinear wires.

7. Conclusion

In conclusion, lithium niobate is a material of current interest in both industry and research, thanks to its robust and reproducible properties and also thanks to the emergence of new technologies such as ion slicing or optical grade dicing. Hence, and even though the first modulators date from the 1970s, progress is still visible, to move toward ever more compactness with low energy consumption and low losses. In this chapter, we have taken particular interest in three important parameters: the Γ electro-optical overlap coefficient that characterizes EO efficiency, the η overlap integral with optical fibers, which quantifies coupling losses, and the propagation losses, the last two parameters being important contributors to overall insertion losses. We have shown how the use of confined guides (deep ridges or thin films) increases the EO efficiency by a factor of 2 and how tapers allow low integration losses. Finally, we have highlighted the spectacular effects of nanostructuring in confined guides to gain 1–2 orders of magnitude on the EO efficiency. These developments open the way toward compact and low-consuming photonic integrated circuit but also offer the promise of multi-control in optical circuits.

Acknowledgements

This work was supported by the SATT Grand-Est under project μguide, partially by ANR under project ANR-16-CE24-0024-01, and by the Labex ACTION program (contract ANR-11-LABX-01-01). The work was partly supported by the French RENATECH network and its FEMTO-ST technological facility.

Author details

Nadège Courjal[1]*, Maria-Pilar Bernal[1], Alexis Caspar[1], Gwenn Ulliac[1], Florent Bassignot[2], Ludovic Gauthier-Manuel[1] and Miguel Suarez[1]

*Address all correspondence to: nadege.courjal@femto-st.fr

1 FEMTO-ST Institute, Besançon, France

2 FEMTO-Engeeniring, Besançon, France

References

[1] Turner EH. High frequency electro-optic coefficients of lithium niobate. Applied Physics Letters. 1966;**8**:303-306. DOI: 10.1063/1.1754449

[2] Wooten EL, Kissa KM, Yi-Yan A, Murphy EJ, Lafaw DA, Hallemeier PF, Maack D, Attanasio DV, Fritz DJ, McBrien GJ, Bossi DE. A review of lithium niobate modulators for fiber-optic communications systems. IEEE Journal on Selected Topics in Quatum Electronics. 2000;**6**:69-82. DOI: 10.1109/2944.826874

[3] DeRose CT, Enami Y, Loychik C, Norwood RA, Mathine D, Fallahi M, Peyghambarian N, Luo JD, Jen AK-Y, Katheperumal M, Yamamoto M. Pockel's coefficient enhancement of poled electro-optic polymers with a hybrid organic-inorganic sol-gel cladding layer. Applied Physics Letters. 2006;**89**:131102-131105. DOI: 10.1063/1.2357157

[4] Huang C, Bhalla AS, Guo R. Measurement of microwave electro-optic coefficient in $Sr_{0.61}Ba_{0.39}Nb_2O_6$ crystal fiber. Applied Physics Letters. 2005;**86**:211907-211910. DOI: 10.1063/1.1937997

[5] van Raalte JA. Linear electro-optic effect in ferroelectric KTN. Journal of the Optical Society of America. 1967;**57**:671-674. DOI: 10.1364/JOSA.57.000671

[6] Johnston AR, Weingart JM. Determination of the low-frequency linear electro-optic effect in tetragonal $BaTiO_3$. Journal of the Optical Society of America. 1965;**55**:828-834. DOI: 10.1364/JOSA.55.000828

[7] Gooch and Housego, lithium niobate optical crystal. [Internet]. 2017. Available from https://goochandhousego.com/wp-content/uploads/2013/12/LNmatProperties.pdf

[8] Eospace, electro-optic modulators [Internet]. 2017. Available from: http://www.eospace.com/

[9] Aydé R, Gaborit G, Dahdah J, Duvillaret L, Courjal N, Guyot C, Sablong R, Perrier AL, Beuf O. Unbiased electro-optic waveguide as a sensitive nuclear magnetic resonance sensor. IEEE Photonics Technology Letters. 2014;**26**:1266-1269. DOI: 10.1109/LPT.2014.2321099

[10] Photonics iXblue. Polarizing Y-Junction Phase Modulator for fiber optics gyros [Internet]. 2017. Available from: https://photonics.ixblue.com/files/files/pdf/Modulators/Y-JPX-LN_series.pdf

[11] Hsiao HK, Winick KA, Monnier JD, Berger JP. An infrared integrated optic astronomical beam combiner for stellar interferometry at 3-4 μm. Optics Express. 2009;**17**:18489-18500. DOI: 10.1364/OE.17.018489

[12] Newport, faq on electro-optic modulators [Internet]. 2017. Available from: https://www.newport.com/n/electro-optic-modulator-faqs

[13] Chen X, Zhang G, Zeng H, Guo Q, She W. Advances in Nonlinear Optics. Berlin, Boston: Walter de Gruyter GmbH & Co KG; 2015 978-3-11-030449-7

[14] Schmidt RV, Kaminow IP. Metal-diffused optical waveguides in $LiNbO_3$. Applied Physics Letters. 1974;**25**:458-461. DOI: 10.1063/1.1655547

[15] Heidmann S, Ulliac G, Courjal N, Martin G. Characterization and control of the electro-optic phase dispersion in lithium niobate modulators for wide spectral band interferometry applications in the mid-infrared. Applied Optics. 2017;**56**:4153-4157. DOI: 10.1364/AO.56.004153

[16] Thomas F, Heidmann S, de Mengin M, Courjal N, Ulliac G, Morand A, Benech P, Le Coarer E, Martin G. First results in near and mid IR lithium niobate-based integrated optics interferometer based on SWIFTS-Lippmann concept. Journal of Lightwave Technology. 2014;**32**:3736-3742

[17] Burns WK, Klein PH, West EJ. Ti diffusion in Ti:$LiNbO_3$ planar and channel optical waveguides. Journal of Applied Physics. 1979;**50**:6175-6179. DOI: 10.1063/1.325801

[18] Ramaswamy V, Alferness RC, Divino M. High efficiency single-mode fibre to Ti:$LiNbO_3$ waveguide coupling. Electronics Letters. 1982;**18**:30-31. DOI: 10.1049/el:19820022

[19] HC Photonics. (Reversed) Proton Exchange waveguides [Internet]. 2017. Available from: http://www.hcphotonics.com/products2.asp?area=1670&cat=1751&sn=939

[20] Glavas E, Cabrera JM, Townsend PD. A comparison of optical damage in different types of $LiNbO_3$ waveguides. Journal of Physics D: Applied Physics. 1989;**22**:611-616

[21] Suchoski Jr PG, Findakly TK, Ferrar CM, Leonberger FJ. Single-polarization, integrated optical components for optical gyroscopes. Patent US5223911 A; 1989

[22] Jackel JL, Rice CE, Veselka JJ. Proton exchange for high-index waveguides in $LiNbO_3$. Applied Physics Letters. 1982;**41**:607-608. DOI: 10.1063/1.93615

[23] Bortz ML, Fejer MM. Annealed proton-exchanged $LiNbO_3$ waveguides. Optics Letters. 1991;**16**:1844-1846. DOI: 10.1364/OL.16.001844

[24] Chanvillard L, Aschiéri P, Baldi P, Ostrowsky DB, de Micheli M, Huang L, Bamford DJ. Soft proton exchange on periodically poled $LiNbO_3$: A simple waveguide fabrication process for highly efficient nonlinear interactions. Applied Physics Letters. 2000;**76**:1089-1091. DOI: 10.1063/1.125948

[25] Suchoski PG, Findakly TK, Leonberger FJ. Stable low-loss proton-exchanged $LiNbO_3$ waveguide devices with no electro-optic degradation. Optics Letters. 1988;**13**:1050-1052. DOI: 10.1364/OL.13.001050

[26] Kaminow IP, Ramaswamy V, Schmidt RV, Turner EH. Lithium niobate ridge waveguide modulator. Applied Physics Letters. 1974;**24**:622-625. DOI: 10.1063/1.1655079

[27] Noguchi K, Mitomi O, Miyazawa H, Seki S. A broadband Ti:LiNbO3 optical modulator with a ridge structure. Journal of Lightwave Technology. 1995;**13**:1164-1168. DOI: 10.1109/50.390234

[28] Noguchi K, Mitomi O, Miyazawa H. Millimeter-wave Ti:$LiNbO_3$ optical modulators. Journal of Lightwave Technology. 1998;**16**:615-620. DOI: 10.1109/50.664072

[29] Laurell F, Webjorn J, Arvidsson G, Holmberg J. Wet etching of proton-exchanged lithium niobate—A novel processing technique. Journal of Lightwave Technology. 1992;**10**:1606-1609. DOI: 10.1109/50.184899

[30] Barry IE, Ross GW, Smith PGR, Eason RW. Ridge waveguides in lithium niobate fabricated by differential etching following spatially selective domain inversion. Applied Physics Letters. 1999;**74**:1487-1490. DOI: 10.1063/1.123589

[31] Hu H, Ricken R, Sohler W. Low-loss ridge waveguides on lithium niobate fabricated by local diffusion doping with titanium. Applied Physics B. 2010;**98**:677-679. DOI: 10.1007/s00340-010-3908-y

[32] Mizuuchi K, Sugita T, Yamamoto K, Kawaguchi T, Yoshino T, Imaeda M. Efficient 340-nm light generation by a ridge-type waveguide in a first-order periodically poled MgO: $LiNbO_3$. Optics Letters. 2003;**28**:1344-1346. DOI: 10.1364/OL.28.001344

[33] Kou R, Kurimura S, Kikuchi K, Terasaki A, Nakajima H, Kondou K, Ichikawa J. High-gain, wide-dynamic-range parametric interaction in Mg-doped $LiNbO_3$ quasi-phase-matched adhered ridge waveguide. Optics Express. 2011;**19**:11867-11872. DOI: 10.1364/OE.19.011867

[34] Umeki T, Tadanaga O, Asobe M. Highly efficient wavelength converter using direct-bonded PPZnLN ridge waveguide. IEEE Journal of Quantum Electronics. 2010;**46**:1206-1213. DOI: 10.1109/JQE.2010.2045475

[35] Chauvet M, Henrot F, Bassignot F, Devaux F, Gauthier-Manuel L, Pêcheur V, Maillotte H, Dahmani B. High efficiency frequency doubling in fully diced $LiNbO_3$ ridge waveguides on silicon. Journal of Optics. 2016;**18**:085503. DOI: 10.1088/2040-8978/18/8/085503/meta

[36] NTT. Wavelength Conversion Module for Visible, Near-IR, and Mid-IR Light Generation [Internet]. Available from https://www.ntt-electronics.com/en/products/photonics/conversion_module.html

[37] Courjal N, Guichardaz B, Ulliac G, Rauch J-Y, Sadani B, Lu H, Bernal M-P. High aspect ratio lithium niobate ridge waveguides fabricated by optical grade dicing. Journal of Physics D: Applied Physics. 2011;**44**:305101. DOI: 10.1088/0022-3727/44/30/305101

[38] Gerthoffer A, Guyot C, Qiu W, Ndao A, Bernal M-P, Courjal N. Strong reduction of propagation losses in $LiNbO_3$ ridge waveguides. Optical Materials. 2014;**38**:37-41. DOI: 10.1016/j.optmat.2014.09.027

[39] Caspar A, Ulliac G, Suarez M, Calero V, Bernal M-P, Courjal N, Roussey M, Häyrinen M, Laukkanen J, Honkanen S, Kuittinen M. High-aspect-ratio electro-optical ridge waveguide made by precise dicing and atomic layer deposition. 2017 Conference on Lasers and Electro-Optics Europe & European Quantum Electronics Conference (CLEO/Europe-EQEC); Munich. 2017. pp. 1–1. DOI: 10.1109/CLEOE-EQEC.2017.8086602

[40] Courjal N, Devaux F, Gerthoffer A, Guyot C, Henrot F, Ndao A, Bernal M-P. Low-loss $LiNbO_3$ tapered-ridge waveguides made by optical-grade dicing. Optics Express. 2015;**23**:13983-13990. DOI: 10.1364/OE.23.013983

[41] Levy M, Osgood RM Jr, Liu R, Cross LE, Cargill GS, Kumar A, Bakhru H. Fabrication of single-crystal lithium niobate films by crystal ion slicing. Applied Physics Letters. 1998;**73**: 2293-2296. DOI: 10.1063/1.121801

[42] Poberaj G, Hu H, Sohler W, Günter P. Lithium niobate on insulator (LNOI) for micro-photonic devices. Laser & Photonics Reviews. 2012;**6**:488-503. DOI: 10.1002/lpor.201100035

[43] NanoLN, LiNbO3 thin films [Internet]. 2017. Available from http://www.nanoln.com/en/pinfo.asp?ArticleID=13

[44] Partow Technologies LLC. Ino sliced thin films. [Internet]. 2017. Available from: http://www.partow-tech.com/thinfilms/

[45] Volk MF, Suntsov S, Rüter CE, Kip D. Low loss ridge waveguides in lithium niobate thin films by optical grade diamond blade dicing. Optics Express. 2016;**24**:1386. DOI: 10.1364/OE.24.001386

[46] Guarino A, Poberaj G, Rezzonico D, Degl'Innocenti R, Günter P. Electro-optically tunable microring resonators in lithium niobate. Nature Photonics. 2007;**1**:407-410. DOI: 10.1038/nphoton.2007.93

[47] Chen L, Chen J, Nagy J, Reano R. Highly linear ring modulator from hybrid silicon and lithium niobate. Optics Express. 2015;**23**:13255. DOI: 10.1364/OE.23.013255

[48] Lu H, Sadani B, Courjal N, Ulliac G, Smith N, Stenger V, Collet M, Baida FI, Bernal M-P. Enhanced electro-optical lithium niobate photonic crystal wire waveguide on a smart-cut thin film. Optics Express. 2012;**20**:2974-2981. DOI: 10.1364/OE.20.002974

[49] Geiss R, Saravi S, Sergeyev A, Diziain S, Setzpfandt F, Schrempel F, Grange R, Kley E, Tünnermann A, Pertsch T. Fabrication of nanoscale lithium niobate waveguides for second-harmonic generation. Optics Letters. 2015;**40**:2715-2718. DOI: 10.1364/OL.40.002715

[50] Chen L, Xu Q, Wood G, Reano RM. Hybrid silicon and lithium niobate electro-optical ring modulator. Optica. 2014;**1**:112-118. DOI: 10.1364/OPTICA.1.000112

[51] Courjal N, Caspar A, Calero V, Ulliac G, Suarez M, Guyot, Bernal MP. Simple production of membrane-based $LiNbO_3$ micro-modulators with integrated tapers. Optics Letters. 2016;**41**:5110-5113. DOI: 10.1364/OL.41.005110

[52] Roussey M, Bernal MP, Courjal N, Van Labeke D, Baida FI. Electro-optic effect exaltation on lithium niobate photonic crystals due to slow photons. Applied Physics Letters. 2006; **89**:241110-241113. DOI: 10.1063/1.2402946

[53] Roussey M, Baida FI, Bernal M-P. Experimental and theoretical observations of the slow-light effect on a tunable photonic crystal. JOSA B. 2007;**24**(6):1416-1422. DOI: 10.1364/JOSAB.24.001416

[54] Burr GW, Diziain S, Bernal M-P. The impact of finite-depth cylindrical and conical holes in lithium niobate photonic crystals. Optics Express. 2008;**16**:6302-6316. DOI: 10.1364/OE.16.006302